



Turbidity currents propagating down a slope into a stratified saline ambient fluid

Raphael Ouillon¹ · Eckart Meiburg¹  · Bruce R. Sutherland²

Received: 14 February 2018 / Accepted: 8 March 2019
© Springer Nature B.V. 2019

Abstract

Results are presented from highly resolved three-dimensional simulations of turbidity currents down a shallow slope into a stratified saline ambient, for various stratifications and particle settling velocity configurations. The front velocity is computed and the results are compared directly to experimental data by Snow and Sutherland (J Fluid Mech 755:251–273, 2014) and to an existing scaling law for gravity currents in stratified environments but on flat bottoms, with close agreement. The entrainment velocity of the ambient fluid into the current is computed from the DNS data and shows strong space time variability. The intrusion of the current into the ambient fluid is computed and compared to the experimental results of Snow and Sutherland (2014), an existing scaling law proposed by those authors, and a new model with increasing levels of complexity. The numerical results highlight the sensitivity of scaling tools to the choice of entrainment coefficient and their limitations in low entrainment but high settling rate scenarios. The new, simpler scaling relation for the intrusion depth is shown to be more robust and predictive in such cases. The energy budget of the flow is analysed in order to explain the governing processes in terms of energy transfers, with a focus on energy losses and potential to kinetic energy transfers. Particular attention is given to the Stokes losses with varying settling velocities, which validates the prediction of the concentration in the intrusion depth model introduced.

Keywords Turbidity current · Geophysical flow · Intrusion · Entrainment

✉ Eckart Meiburg
meiburg@engineering.ucsb.edu

Raphael Ouillon
ouillon@engineering.ucsb.edu

Bruce R. Sutherland
bruce.sutherland@ualberta.ca

¹ Department of Mechanical Engineering, University of California, Santa Barbara, USA

² Departments of Physics and of Earth and Atmospheric Sciences, University of Alberta, Edmonton, Canada

1 Introduction

Gravity currents are predominantly horizontal, buoyancy-driven flows of a denser fluid through a lighter fluid. When this density difference is due to the presence of suspended particles, we refer to the flow as a turbidity current. The particles are mainly suspended by turbulence and are subject to sedimentation, so that the buoyancy of the turbidity current is not conserved. The interstitial and ambient fluids are usually miscible, and the ambient fluid can be entrained into the current. The most common fluid involved in turbidity currents is fresh and/or saline water [15]. Turbidity currents play a key role in sediment transport in aquatic environments such as oceans, reservoirs and lakes. They represent the principal means of sediment transport from shallow to deeper waters in the ocean, and they can carry large amounts of sediment over very long distances. Studying their behaviour is therefore essential to understanding the physics governing sediment transport and deposition. The destructive nature of turbidity currents is responsible for substantial damage to submarine engineering infrastructure such as pipelines and telecommunication cables. Predicting the energy content and velocity of turbidity currents is therefore essential for the design of robust engineering structures.

Most studies on turbidity currents to date, both numerical [4, 13] and experimental [7], have considered flows on flat bottoms in constant density ambient fluids. The effects of stratification on the propagation of turbidity currents were investigated experimentally for a two-layer setup [8, 22] or a constant gradient [6], while the effects of a slope were examined for a uniform ambient fluid [21]. While these studies yield important insight into the dynamics of turbidity currents, the combined effects of stratification and sloping bottom are not yet well understood. To that end, Snow and Sutherland [23] conducted a series of experiments of hyperpycnal and hypopycnal turbidity currents down a slope in a linearly stratified saline ambient fluid. The authors discuss the effects of settling velocity and stratification on the qualitative behaviour of the current, and further investigate the changes in front velocity and intrusion depth for various configurations of particle sizes, stratification, and slope angle. Being able accurately to estimate the intrusion depth is paramount, as it corresponds to the point where the turbidity current lifts from the slope and loses much of its destructive potential. It also strongly affects the dynamics of settling by driving the particle-laden current away from the slope. Snow and Sutherland [23] analytically derive a scaling law for the intrusion depth that takes both entrainment and settling of particles into account. The qualitative validity of this law is verified by their experimental results and works well in the limit of short descents (high relative stratification) and long descents (low relative stratification). This scaling law, however, relies on the predictability of the entrainment. A reference entrainment value of $E = 0.05$ or $E = 0.01$, depending on the slope, is found by fitting the intrusion depth scaling law to experimental data for particle-free gravity currents. The entrainment is not measured directly and its relative importance to settling processes is not assessed. The impact of entrainment variability on the quality of the prediction is thus not fully addressed in situations where settling of particles becomes the driving mechanism for changes in current density. By investigating this problem numerically, we are able to monitor the dynamics of the current explicitly and in a time and space resolved manner in order to analyse its velocity, its mixing and its settling behaviour. By doing so, we can show directly the sensitivity of the predicted intrusion depth to the choice of entrainment coefficient in cases of settling-driven currents, and investigate more robust predictive tools for such circumstances.

Finally, the comprehensive data set provided by numerical simulations can be used to analyse the total energy budget and the dynamical energy transfers in such turbidity currents. This analysis of energy transfer rates helps build an understanding of the physical interplay of settling and entrainment and their influence on the dynamics of the current, and it supports the idea of choosing appropriate scaling tools depending on the dominant mechanism.

The initial set-up is sketched in Fig. 1. The density inside the clear ambient fluid increases linearly from ρ_T at the top to ρ_B at the bottom such that

$$\rho_2(y) = \rho_B + (\rho_T - \rho_B) \cdot \frac{y}{H} \tag{1}$$

The channel of width W is homogeneous in the spanwise z -direction. The particle-laden lock region of constant density ρ_1 is initially at rest. At $t = 0$, the lock is released and the particle-laden flow of initial density $\rho_1 > \rho_A$ begins to move down the slope, and to interact with the ambient fluid. The local density of the fluid then depends on the particle concentration c and salinity s .

2 Physical modelling

The problem is governed by the three-dimensional incompressible Navier–Stokes equations. Since the suspensions considered are in the dilute regime with volume fractions well below 1%, particle–particle interactions can be neglected and the fluid and particle motion is dominated by transfer of momentum rather than volumetric displacement. Density variations due to the particles and salinity are sufficiently small for the Boussinesq approximation to hold. The density of the flow is therefore considered to be constant and equal to the reference density ρ_0 , with the exception of the gravity term. The evolution of the particle and salinity concentrations is modelled using an Eulerian approach, based on convection–diffusion equations. Note that the diameter of the particles is assumed to be much

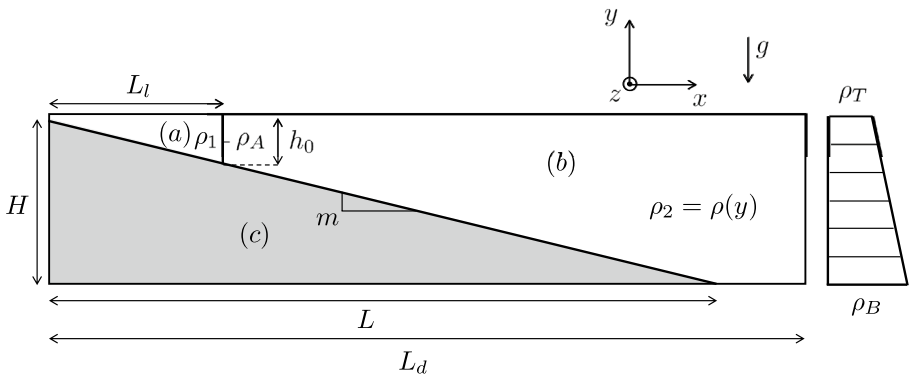


Fig. 1 Problem set-up and configuration. **a** Particle-laden fluid; **b** ambient stratified fluid; **c** solid region. H and L denote the maximum depth and the horizontal extent of the inclined ramp, respectively. L_d is the horizontal length of the domain, h_0 and L_l denote the height and horizontal length of the lock, and m indicates the slope. ρ_1 is the bulk density of the lock, ρ_T is the initial density at the top of the ambient fluid, ρ_B is the initial density at the bottom of the ambient fluid and ρ_A is the initial density in the ambient fluid at half-lock depth

smaller than the smallest length scale of the fluid motion, so that the particle inertia can be neglected and the velocity of the particles is considered to be equal to the sum of the fluid velocity and the particle settling velocity. The particle and salinity velocity fields are therefore divergence free. This approach has previously been successfully employed to investigate numerically the effects of settling on the dynamics of particle-laden flows [19], as well as their dissipation and mixing properties [20]. It was also used to study the effects of bottom topography on the mixing dynamics of turbidity currents [18]. The governing equations and choice of non-dimensional parameters are described in depth by Necker et al. [19], so that they will be summarized only briefly here.

The non-dimensional continuity, momentum, particle transport and salt transport equations are given by

$$\nabla \cdot \mathbf{u} = 0, \tag{2}$$

$$\frac{\partial \mathbf{u}}{\partial t} + (\mathbf{u} \cdot \nabla) \mathbf{u} = -\nabla p + \frac{1}{Re} \Delta \mathbf{u} + (\alpha_s s + \alpha_c c) \mathbf{e}_y, \tag{3}$$

$$\frac{\partial c}{\partial t} + (\mathbf{u} + \mathbf{v}_s) \cdot \nabla c = \frac{1}{Re Sc_c} \Delta c, \tag{4}$$

$$\frac{\partial s}{\partial t} + \mathbf{u} \cdot \nabla s = \frac{1}{Re Sc_s} \Delta s, \tag{5}$$

where \mathbf{u} , p , s , c represent the non-dimensional fluid velocity, pressure, salinity and particle concentration, respectively. With $(\tilde{\cdot})$ referring to variables in their dimensional form, we define the Reynolds number Re as

$$Re = \frac{\tilde{u}_b \tilde{H}}{\tilde{\nu}}, \tag{6}$$

where $\tilde{\nu}$, \tilde{H} and \tilde{u}_b , respectively, denote the kinematic viscosity, the maximum depth (see Fig. 1) and the buoyancy velocity

$$\tilde{u}_b = \sqrt{\tilde{g}' \tilde{h}_0} = \sqrt{\frac{\tilde{\rho}_1 - \tilde{\rho}_A}{\tilde{\rho}_0} \tilde{g} \tilde{h}_0}. \tag{7}$$

here $\tilde{\rho}_1$ is the initial lock density, $\tilde{\rho}_A$ denotes the initial ambient fluid density at mid-lock height, and $\tilde{\rho}_0$ indicates the interstitial fluid density. The variables are made non-dimensional by choosing \tilde{H} and \tilde{u}_b as the flow reference scales such that $\mathbf{x} = \frac{\tilde{\mathbf{x}}}{\tilde{H}}$, $\mathbf{u} = \frac{\tilde{\mathbf{u}}}{\tilde{u}_b}$, $t = \frac{\tilde{t}}{\tilde{H}/\tilde{u}_b}$, $p = \frac{\tilde{p}}{\tilde{\rho}_0 \tilde{u}_b^2}$. The settling velocity is obtained by balancing the gravitational forces with the Stokes drag of a sphere in a flow of uniform velocity such that $\mathbf{v}_s = -\frac{\tilde{v}_s}{\tilde{u}_b} \mathbf{e}_y$, with

$$\tilde{v}_s = \frac{d_p^2 (\tilde{\rho}_p - \tilde{\rho}_0) \tilde{g}}{18 \tilde{\rho}_0 \tilde{\nu}}. \tag{8}$$

The particle concentration and salinity fields are made non-dimensional as $c = \frac{\tilde{c}}{c^*}$ and $s = \frac{\tilde{s}}{s^*}$, where $c^* = \tilde{\rho}_p \frac{\tilde{\rho}_1 - \tilde{\rho}_0}{\tilde{\rho}_p - \tilde{\rho}_0}$ and $s^* = \tilde{\rho}_s \frac{\tilde{\rho}_B - \tilde{\rho}_0}{\tilde{\rho}_s - \tilde{\rho}_0}$. Here $\tilde{\rho}_p$ is the density of particles, $\tilde{\rho}_s$ is the

density of salt and $\tilde{\rho}_B$ is the density at the bottom of the channel. In this way the non-dimensional particle and salt expansion coefficients are given by

$$\alpha_c = \frac{\tilde{\rho}_1 - \tilde{\rho}_0}{\tilde{\rho}_1 - \tilde{\rho}_A} \frac{\tilde{H}}{\tilde{h}_0},$$

$$\alpha_s = \frac{\tilde{\rho}_B - \tilde{\rho}_0}{\tilde{\rho}_1 - \tilde{\rho}_A} \frac{\tilde{H}}{\tilde{h}_0}.$$

The particle and salt Schmidt numbers, Sc_c and Sc_s , are defined, respectively, as

$$Sc_c = \frac{\tilde{\nu}}{\tilde{\kappa}_c}, \quad Sc_s = \frac{\tilde{\nu}}{\tilde{\kappa}_s}. \tag{9}$$

For the sake of simplicity, and in following earlier authors, the diffusivity coefficients are chosen to be equal to the kinematic viscosity such that $\tilde{\kappa}_s = \tilde{\kappa}_c = \tilde{\nu}$, leading to

$$Sc_s = Sc_c = 1. \tag{10}$$

Note that while the real values of Sc_c and Sc_s are much larger than unity, the effect of molecular diffusivity on the propagation of the current in such a turbulent, high Reynolds flow, are negligible as long as $Sc \geq 1$ [10]. The Schmidt number also does not impact the destabilization of the initially two-dimensional flow through the lobe-and-cleft instability as long as $Sc \geq 1$ [12]. In order to discuss the effects of stratification, it is convenient to define a buoyancy frequency N that expresses the characteristic frequency at which a fluid would vertically oscillate in a stably stratified environment. When using the Boussinesq approximation, this is defined as

$$\tilde{N} = \sqrt{\tilde{g} \frac{\tilde{\rho}_B - \tilde{\rho}_T}{\tilde{\rho}_T \tilde{H}}}, \tag{11}$$

where $\tilde{\rho}_T$ and $\tilde{\rho}_B$ are the initial ambient fluid densities at the top and bottom of the channel, respectively. In its non-dimensional form, this can be expressed as

$$N = \tilde{N} \cdot \frac{\tilde{H}}{\tilde{u}_b}. \tag{12}$$

This non-dimensional buoyancy frequency compares the time-scale associated with stratification to the time-scale associated with the propagation of the current down to the bottom of the channel. It is therefore difficult to interpret. We therefore use the stratification magnitude S instead, defined as

$$S \equiv \frac{\tilde{\rho}_{h_0} - \tilde{\rho}_T}{\tilde{\rho}_1 - \tilde{\rho}_T}. \tag{13}$$

The above equations are solved via our immersed boundary code TURBINS [17]. Slip boundary conditions are employed at the top and right walls, and periodic conditions are implemented on the lateral boundaries. The width of the domain is chosen sufficiently large so that the periodic boundary conditions do not have a significant impact on the flow. An immersed boundary method is used to impose the no-slip condition on the slope ($\mathbf{u}|_{\Gamma_s} = 0$) [14, 16, 17]. In order to impose the boundary conditions, immersed boundary methods

add a body force \mathbf{f} to the Navier–Stokes equations. This force is evaluated by requiring that the velocity on the boundary $\mathbf{u}|_{\Gamma_s}$ is equal to the desired boundary velocity \mathbf{v}_{Γ_s} . If the grid node coincides with the boundary on which the condition is imposed, the forcing term is exact. This is of course rarely the case and interpolation methods are required to impose proper forces on the near-boundary nodes. Fadlun et al. [9], Kang [14], Nasr-Azadani and Meiburg [17] and Tseng and Ferziger [24] provide more details about the computation of the body force and its interpolation.

3 Flow structure and behaviour

3.1 General considerations

The numerical simulations aim at reproducing the experiments conducted by Snow and Sutherland [23] and at conducting parametric studies on the settling velocity v_s and stratification parameter S . Table 1 summarizes the parameters for a selection of simulations. In addition, a parametric study on the Reynolds number was conducted and demonstrated that the variables of interest converge for sufficiently large values of Re . In other words, the Reynolds number did not influence the results as long as the flow quickly became fully turbulent (typically $Re > 6000$ in the simulations).

The representative behaviour of a lock-release turbidity current down a slope into a stratified ambient fluid is shown in Fig. 2. The spanwise-averaged particle concentration is represented on a linear grey scale for various times throughout the simulation. The concentration varies between $c = 0$ and $c = 1$, where we recall that the concentration is made non-dimensional by the initial lock fluid concentration. Upon extraction of the model-gate, the flow starts to move down the slope. Soon Kelvin–Helmholtz rollers form which subsequently break down into fully three-dimensional turbulence, thereby creating smaller dissipative vortices as observed at later times ($t > 10$).

The influence of the ambient fluid stratification becomes evident at later times ($t \approx 15$) when the current separates from the surface of the ramp and intrudes into the ambient fluid. The effects of stratification on intrusion depth are key in understanding the evolution of the suspended mass, deposit profiles and energy budgets, as will be discussed later.

In most of the experiments conducted by Snow and Sutherland [23], the Reynolds number $Re = \frac{\bar{u}_b H}{\nu}$ exceeds 15,000. They observed turbulent mixing along the whole length of the current at its interface with the ambient fluid. Numerical simulations

Table 1 Summary of relevant simulations

	exp1	exp2	exp3	S sensitivity	v_s sensitivity
Re	16,850	15,000	35,000	15,000	15,000
S	0.653	0.176	0.248	0, 0.419, 0.692, 0.885, 1.028	0.419
v_s	0.00731	0.00108	0.000463	0.001	0, 0.001, 0.005, 0.01
m	0.149	0.149	0.149	0.0744	0.0744

exp1,2,3 reproduce experiments by Snow and Sutherland [23]. The parametric studies on the stratification S and settling velocity v_s are based on realistic lab scale physical parameters and represent a small sample of the total body of simulations that were conducted

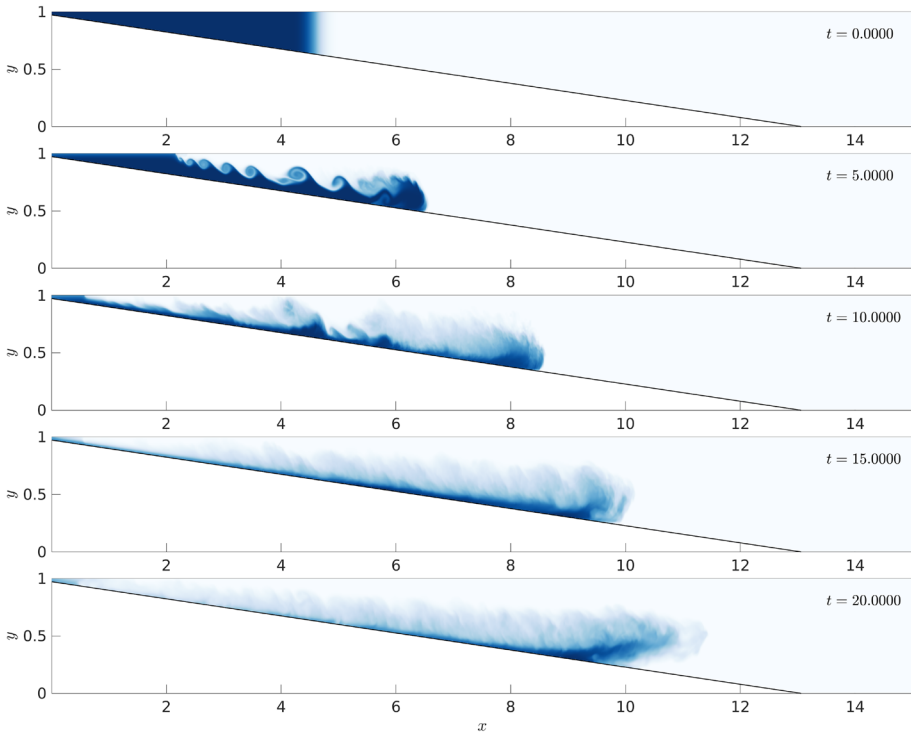


Fig. 2 Spanwise averaged particle concentration field for various times ($Re = 15,000$, $\nu_s = 0.001$, $S = 0.419$, $m = 0.0744$). A 2:1 aspect ratio is used to improve readability

corroborate this behaviour as illustrated in Fig. 2. In the experiments, the lock is stirred before release to guarantee a homogeneous suspension of particles. This introduces initial turbulence that contributes to the rapid destabilisation of the flow. In our simulations a small random perturbation is applied to the initial velocity field, such that the lobe-and-cleft instability, initiated at the head of the current, quickly propagates along the body of the current thus destabilizing the large Kelvin–Helmholtz rollers formed



Fig. 3 Snapshots of a turbidity current experiment (exp2, based on experiments by Snow and Sutherland [23], $S = 0.176$, $Re = 15,000$, $\nu_s = 0.001$, $m = 0.149$) right before separation of the current from the bottom slope. Experimental results (top) and the corresponding numerical results are compared at time $t = 12.1$

after release of the lock fluid. Figure 3 compares the 2D averaged concentration field between the experiments and the simulations for a typical turbidity current.

4 Dynamic flow properties

4.1 Front velocity

The front velocity refers to the along-slope velocity of the head of the current. It is proportional to the time derivative of the position of the front x_f defined using a concentration threshold c_{lim} as the furthest point on the slope that verifies $c(x_f, y_s(x_f)) > c_{lim}$, where $y_s(x_f)$ is the y -position of the the forward-most point of the front. Note that here we employ the spanwise averaged concentration used, in order to be consistent with the definition of [23]. The concentration threshold is chosen as $c_{lim} = 0.05$, i.e. 5% of the initial lock concentration. We note that the concentration gradient at the head of the current in the direction of propagation is strong, so that the result for the front velocity is independent of the choice of c_{lim} . The front velocity U_f is then computed as

$$U_f = \frac{1}{\cos \theta} \frac{dx_f}{dt}, \quad (14)$$

where θ is the angle of the slope. The front velocity for various settling velocities v_s is represented as a function of time in Fig. 4a ($Re = 15,000$, $v_s = 0.001$, $m = 0.0744$). After release, the front rapidly accelerates before an abrupt decrease in acceleration ($t \approx 2$) to a small but finite value. This behaviour differs from the inertial phase that follows the acceleration phase of planar gravity currents [5] in that the current does not reach a constant velocity after the acceleration phase. The geometry of the lock and the varying depth of the ambient fluid with the slope contribute to this behaviour [26]. In this secondary

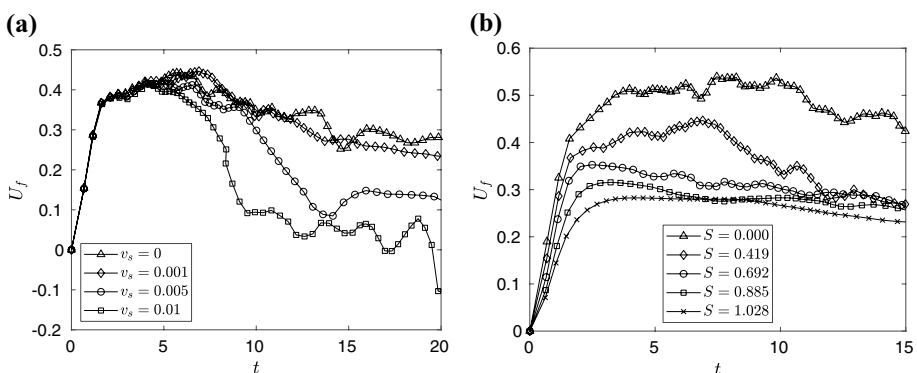


Fig. 4 **a** Front velocity as a function of time for various settling velocities v_s ($Re = 15,000$, $S = 0.419$, $m = 0.0744$). Larger settling velocities lead to a more rapid drop in the density of current and thus decrease the time before intrusion. As intrusion occurs, the front velocity drops dramatically, and it can even oscillate around zero near the intrusion point. This is observed for $v_s = [0.005, 0.01]$ during the interval $t \sim [11, 19]$ respectively. **b** Front velocity as a function of time for various stratifications S ($Re = 15,000$, $v_s = 0.001$, $m = 0.0744$). An increase in stratification reduces the front's acceleration and its velocity plateau as less potential energy is available overall for conversion into kinetic energy

acceleration phase however, the front velocity increases slowly and is approximated in the following by a Froude number defined as the average of the front velocity

$$\text{Fr} = \bar{U}_f(t_s < t < t_i) \quad (15)$$

where t_s and t_i are the time at the onset of the slow acceleration phase and the time when intrusion begins, respectively.

As the current is about to intrude in the ambient fluid, the front velocity decreases. Some of the fluid from the current close to the slope can then move back up the slope while the rest intrudes and moves horizontally away from the slope at a slower velocity than before intrusion, as seen in Fig. 4a. Note that the definition of the front velocity based on the rightmost location of the current differs from that of Snow and Sutherland [23] who extract the current location slightly above the slope and differentiate it to find the front velocity. Both definitions are consistent until intrusion where the rightmost location of the current becomes part of the intrusion but the current above the slope slows down to a halt. In the experiments, a similar increase in front velocity followed by a relatively constant front velocity is observed. As intrusion occurs, the backward motion of the current right above the slope is also observed. This can be seen in figure 6 of Snow and Sutherland [23] where the along-slope position of the front of the current is seen to oscillate around a maximum reached at intrusion. Before intrusion, it can be seen that the settling velocity has very little impact on the front velocity. The loss in head density due to settling decreases the density difference between the current and the ambient fluid and the front velocity is therefore slightly diminished by an increase in settling velocity, but this influence is small within the parameter range investigated here.

Stratification has a much stronger influence on the front velocity during and after the first acceleration phase. Figure 4b represents the front velocity as a function of time for various stratifications S . The increase in the front velocity during the acceleration phase is related to the amount of kinetic energy that can be created from the initial lock configuration, which depends on the potential energy initially stored in the lock. It can be inferred that the front acceleration is related to the density difference between the lock and the ambient fluid at the bottom of the lock, i.e. $\tilde{\rho}_1 - \tilde{\rho}_{h_0}$ and thus that acceleration decreases with S . The change in front velocity after the initial acceleration phase depends on stratification, with slowly accelerating fronts for $S = [0, 0.419]$ and slowly decelerating fronts for $S = [0.692 - 1.028]$, suggesting that stratification also contributes to the difference in behaviour when compared to a classic planar gravity current [5]. Figure 5 presents the current simulation results, along with the experimental data of Snow and Sutherland [23], for the Froude number Fr as a function of stratification S . The experimental and numerical data are compared to theoretical predictions of Fr in the limits of no stratification ($S = 0$) and strong stratification ($S = 1$) as presented by Ungarish [25]. The author investigated a generalization of the work of Benjamin [2] to a steady gravity current propagating into a linearly stratified ambient fluid on a flat bottom. A flow-field solution of Long's model is combined with a flow-force balance over the width of the channel to yield solutions for the Froude number. We observe that the simulation data fall within the error bars of the experimental results. In the absence of stratification, the simulation results yield a Froude number of $\text{Fr} = 0.496$, which closely matches the theoretical value of $\text{Fr} = 0.5$. At $S = 1.028$, the Froude number decreases to $\text{Fr} = 0.2645$, which agrees well with the theoretical value of $\text{Fr} = 0.25$ at $S \approx 1$.

The dependence of Fr on the current to channel height ratio h_c/H is not clearly defined in the case of a sloping bottom with a flat top interface, so that the direct application of this relationship to the present set-up is not straightforward [25]. However, comparing the results of

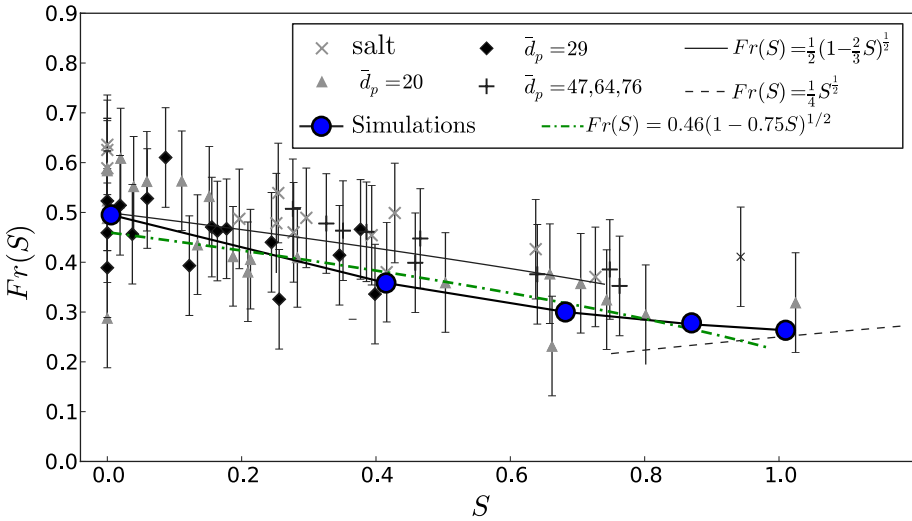


Fig. 5 Froude number as a function of stratification—comparison with the experimental data of [23]. The numerical results are seen to fall within the margin of error of the experimental data. In the limit of no stratification ($S = 0$), the numerical simulations recover the theoretical limit of $Fr = 0.5$, and they approach the asymptotic value of $Fr = 0.25$ as $S \rightarrow 1$. Possible explanations for the wide spread of experimental results are the variability in initial turbulent kinetic energy contained in the lock due to stirring, as well as uncertainties introduced by the release of the gate

the numerical simulations to a prediction of an effective Froude number in a stratified ambient proposed by [26] yields very satisfactory agreement (Fig. 5). This effective Froude number is given, in the present geometry, by $Fr_e = 0.46(1 - 0.75S)^{0.5}$. This observation reaffirms that for small slopes (typically less than 10°), the slope does not impact the characteristics of the current [1, 3].

4.2 Entrainment

Entrainment of ambient fluid into the current, or detrainment of interstitial fluid from the current into the ambient fluid, contribute to the change in current density and play an important role in the intrusion phenomenon. Various approaches can be used to estimate entrainment, such as the box model description [23], which results in a constant value for the entrainment rate, independent of time and space. A time and space-resolved approach is considered here, based on the DNS simulation results. A local entrainment velocity $U_e(x, t)$ is explicitly computed at each point along the x -direction, which avoids the constant entrainment assumption made by [23].

Firstly, the top and bottom positions $y_{top}(x, t)$ and $y_{bot}(x, t)$ of the current are computed using a concentration threshold $c_{lim} = 0.01$. We note that the results are relatively independent of the choice of c_{lim} , in the sense that varying it by a factor of 50 from 0.001 to 0.05 typically results in a change of the entrainment velocity of less than 10%. The local volume flux balance is computed as

$$U_e(x, t) = \frac{\partial q_i(x, t)}{\partial x} = \frac{\partial}{\partial x} \int_{y_{bot}(x, t)}^{y_{top}(x, t)} (u(x, y, t) \cdot \cos \theta + v(x, y, t) \cdot \sin \theta) dy \quad (16)$$

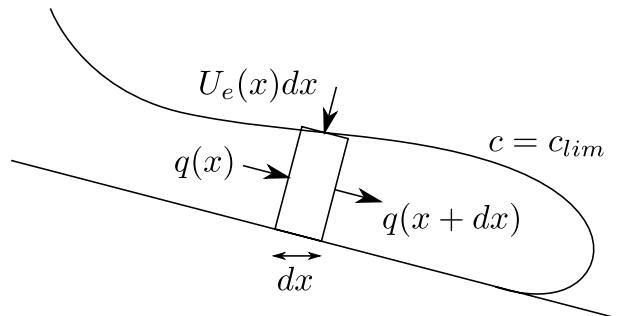
where $U_e(x)$ is the entrainment velocity and $q_f(x)$ is the volume flux of the current at point x , cf. Fig. 6. The above is based on the spanwise averaged two-dimensional data. The dimensionless local rate of entrainment $E(x)$ is then computed as the ratio of the local entrainment velocity to the front velocity such that

$$E(x, t) = \frac{U_e(x, t)}{U_f(t)}. \tag{17}$$

In the present investigation, we evaluated the entrainment rate for a simulation of a set-up that corresponds to one of the experiments of [23]. The Reynolds number is $Re = 15,000$, the settling velocity is $v_s = 0.001077$, the stratification is $S = 0.176$ and the slope is $m = 0.149$. Figure 7a represents a map of the computed entrainment velocity U_e as a function of both space and time. At time $t \approx 5$ (corresponding to a front location of $x_f \approx 2L_l$, where L_l is the lock-length), the flow starts destabilising and strong mixing occurs in a well defined turbulent zone behind the head of the current. Following this destabilization, one can observe the emergence of two regions of strong entrainment that evolve and spread until the intrusion forms around $t = 10$, corresponding to $x_f \approx 3L_l$. These distinct regions of high mixing can be easily understood by looking at the particle concentration in the domain as shown in Fig. 7c. The current boundary, computed using a concentration limit of $c_{lim} = 0.01$, is indicated in the figure. The current exhibits two thickness maxima behind the head that correspond to highly dissipative regions where mixing is much stronger than in the rest of the current. These regions correspond to the two high entrainment zones seen in Fig. 7a at corresponding times. Similar observations can be made at later times when more than 2 regions of high entrainment appear. This is seen in Fig. 7d, which shows the particle concentration and current boundary at $t = 9$, right before intrusion. Three regions of strong mixing are present, which can be identified by the two bumps in particle concentration in the tail of the current and the head itself.

These observations confirm the non-uniform nature of entrainment along the body of the current. Figure 7b shows the evolution with time of the entrainment E averaged on the length of current. There is a good match between the assumed entrainment of $E = 0.05$ in the experimental paper of [23] and the computed entrainment value of $E = 0.061$, averaged along the current. Furthermore, the computed entrainment value agrees closely with experimental observations for a current propagating over a flat surface of $E = 0.063 \pm 0.003$ [11]. Nonetheless, the numerical results highlight the strong variability of entrainment in both time and space when stratification and a slope are present. These affect the structure of the current, and thereby change the mixing patterns along its tail.

Fig. 6 Local control volume employed to define the entrainment velocity. The balance is applied on a differential volume of length dx at location x . The envelope of the current that determines the height of the differential volume is defined based on a threshold concentration $c_{lim} = 0.01$



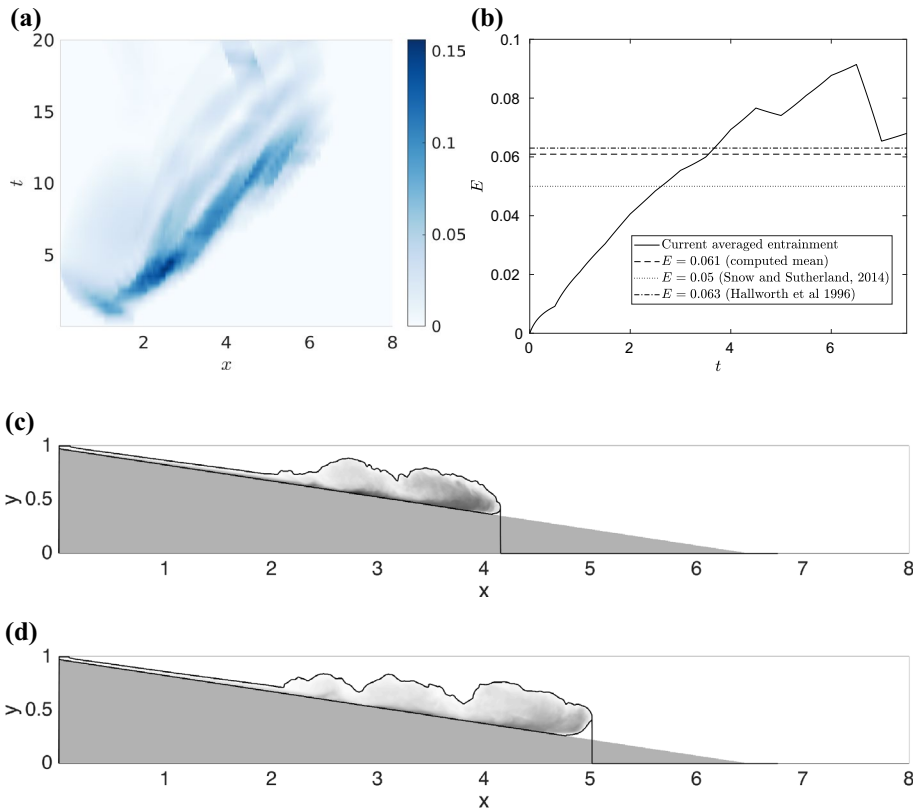


Fig. 7 ($Re = 15,000$, $\nu_s = 0.001077$, $m = 0.149$ and $S = 0.176$). **a** Entrainment velocity U_e mapped as a function of time and horizontal position. **b** Entrainment averaged along the length of the current before intrusion as a function of time. The time averaged value of $E = 0.061$ is plotted and compared to the values of $E = 0.063$ [11] and $E = 0.05$ [23], showing good agreement on average, but highlighting the variability of E with time. Spanwise averaged particle concentration at $t = 6$, and **d** $t = 9$. The concentration contour $c = c_{lim} = 0.01$ is drawn to visualize the envelope of the current, revealing regions of larger entrainment in the body of the current

4.3 Intrusion depth

The intrusion depth H_i is the depth at which the current lifts from the slope. This occurs when the density in the head of the current equals the local density of the ambient fluid. Consistent with [23], this depth is computed as the lowest point at a height $h^* = 0.5$ cm above the slope that reaches a certain threshold concentration value c_{lim} . Naturally, we expect H_i to depend on the stratification. Figure 8a shows the spanwise averaged particle concentration at $t = 15$ for various stratifications S , in a configuration based on the experiments by Snow and Sutherland [23]. The dashed line indicates the location of the calculated intrusion depth. Note that the value c_{lim} influences the results more so when the head of the current is diluted, and that the lowest point reached by the current before intrusion can be lower than the intrusion itself due to the inertia of the fluid. Visual representation of the measured intrusion depth is thus important to validate its calculation. The increase in buoyancy frequency, or stratification, leads to a decrease in intrusion depth. The flow

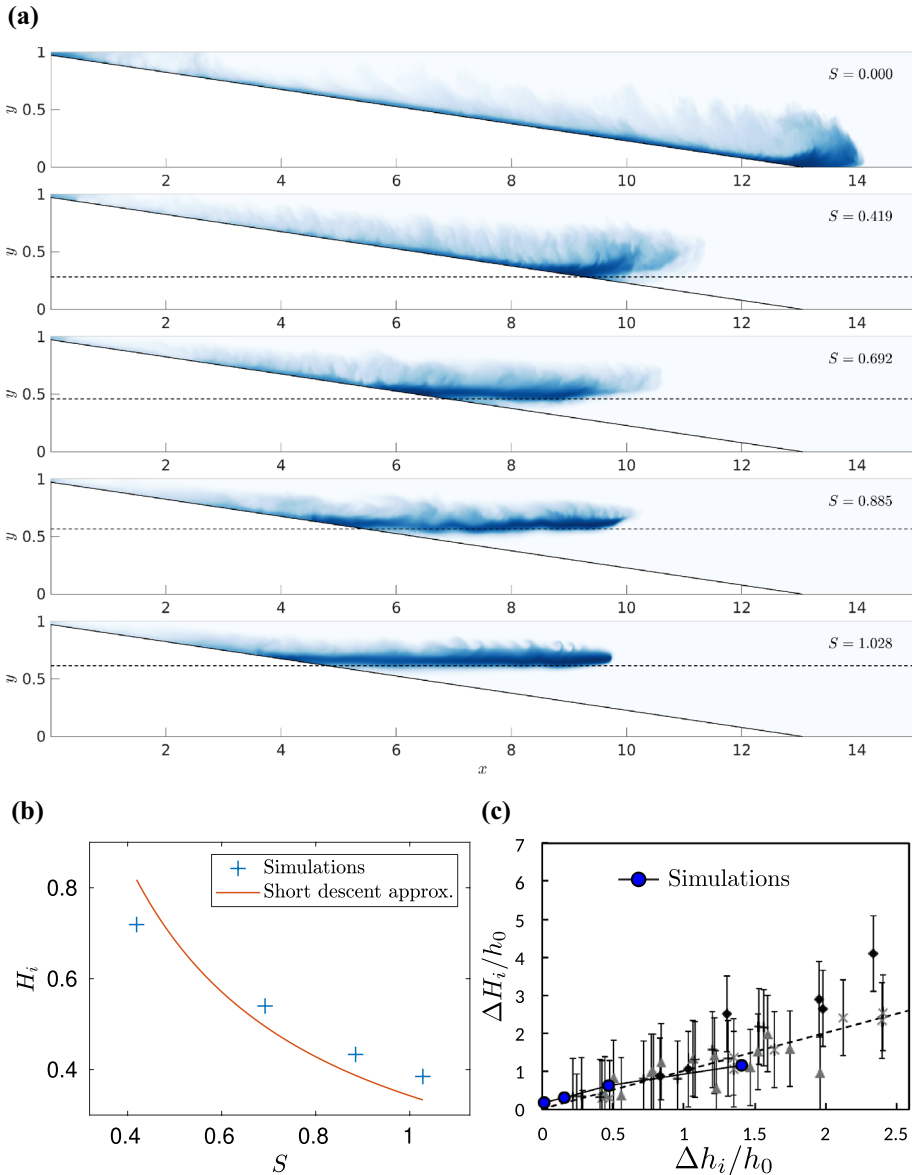


Fig. 8 $Re = 15,000$, $m = 0.0744$, $v_s = 0.001$, $S = 0.419, 0.692, 0.885, 1.028$. **a** Particle concentration for various stratifications S at $t = 15$. As the stratification is increased, intrusion occurs earlier and at a lower depth in the channel. **b** Intrusion depth H_i as a function of stratification S . For such a settling velocity, the short descent approximation agrees very well with simulation results even at moderately large stratification. **c** Relative intrusion depth $\Delta H_i/h_0 = (H_i - h_0)/h_0$ for experimental and numerical data as a function of the predicted relative intrusion depth $\Delta h_i/h_0 = (h_i - h_0)/h_0$ using the short descent approximation. The dashed-line corresponds to perfect agreement. Simulation results are superimposed onto the experimental results of figure 10b of Snow and Sutherland [23] and show close agreement with the short descent approximation, as well as with the experimental data

Fig. 9 $Re = 15,000$, $S = 0.419$, $m = 0.0744$. **a** Particle concentration for various settling velocities v_s at $t = 15$. **b, c** Top: Intrusion depth H_i as a function of the settling velocity v_s . The simulation results are compared to the short descent approximation (SD), the long descent approximation (LDA) introduced by Snow and Sutherland [23], as well as the presented homogeneous settling approximations HS, HSE and HSEC. The LDA, HSE and HSEC are computed using $E = 0.01$ (**b**) and $E = 0.002$ (**c**). Bottom: Relative error $\epsilon = \frac{H_i - h_i}{H_i}$ where h_i is the approximation of H_i using LDA, HS, HSE and HSEC with $E = 0.01$ (**b**) and $E = 0.002$ (**c**)

intrudes earlier and higher along the slope, it propagates more slowly, and its particle concentration is higher.

For very strong stratification, the current is expected to intrude quickly after release. Under those conditions, the influence of entrainment and particle settling can be neglected, so that we can assume the current density at intrusion to be equal to its initial lock density ρ_1 . Omitting the \tilde{A} , this yields

$$\rho_1 = \rho_T + (\rho_B - \rho_T) \frac{H_i}{H}. \tag{18}$$

This yields an expression for the non-dimensional intrusion depth

$$\frac{H_i}{H} = \frac{\rho_1 - \rho_T}{\rho_B - \rho_T}, \tag{19}$$

which can be expressed as a function of the stratification such that

$$H_i = \frac{\rho_1 - \rho_T}{\rho_B - \rho_T} = \frac{\rho_1 - \rho_T}{(\rho_B - \rho_T) \frac{h_0}{H}} = \frac{1}{S} \cdot \frac{h_0}{H}. \tag{20}$$

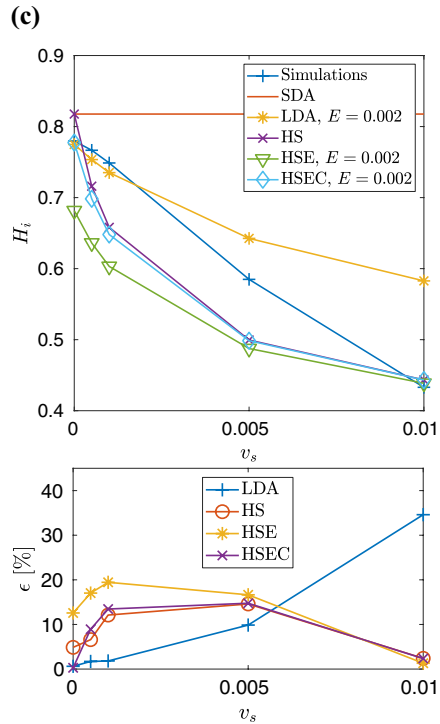
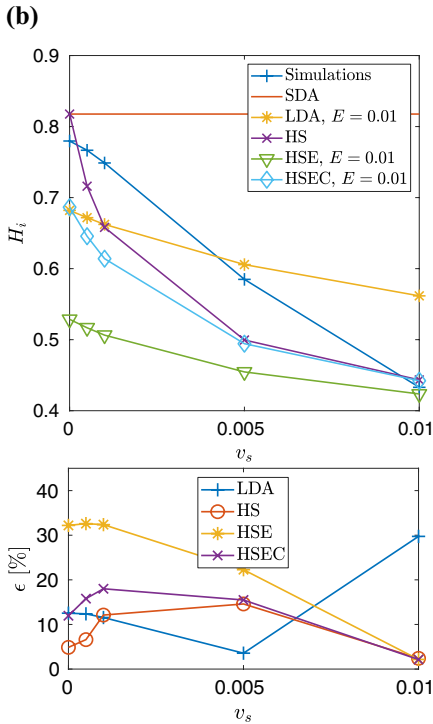
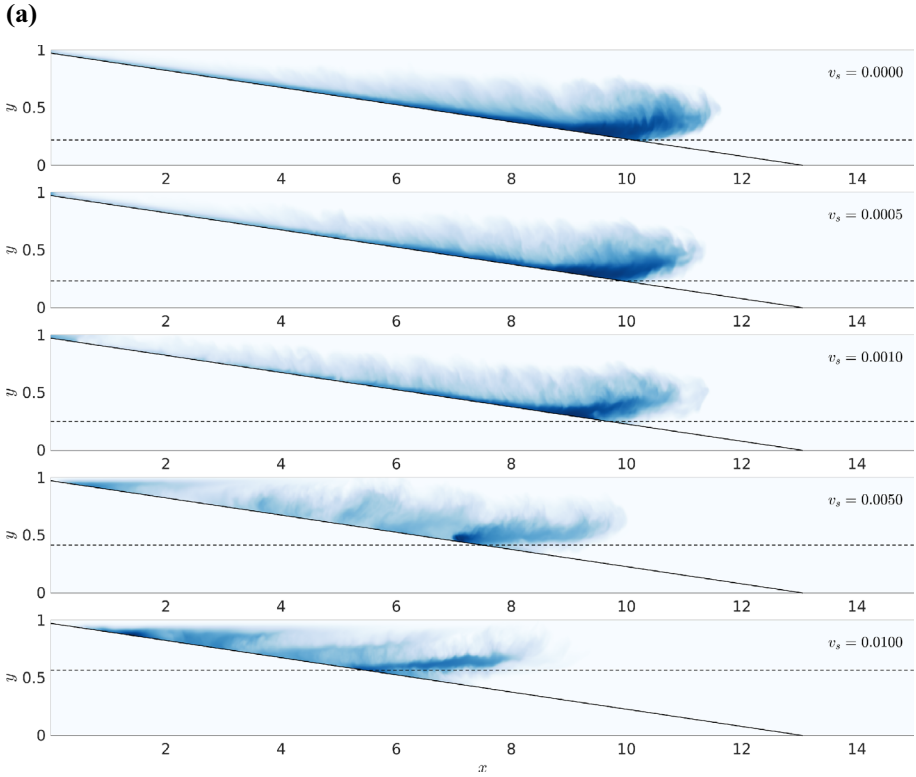
This constitutes a short-descent approximation of the intrusion depth. Applying this relationship to the case of Fig. 8a, the intrusion depth H_i as a function of stratification S can be compared to the approximation (Fig. 8b). The short descent approximation matches the simulation results well in trend and quantitatively. The approximation slightly underestimates the intrusion depth for strong stratification, but the difference remains smaller than the thickness of the current itself. Weaker stratifications would lead to longer run-out lengths, which are prohibited by the size of the domain. For the smallest stratification tested however, the short descent approximation overestimates the intrusion depth and is expected to do so as entrainment and settling effects become more important with longer running currents.

Simulation data were also compared to experimental data from Snow and Sutherland [23] and directly plotted against the short descent approximation, in Fig. 8c. The figure shows the relative intrusion depth defined as

$$\frac{\Delta H_i}{h_0} = \frac{H_i - h_0}{h_0} \tag{21}$$

as a function of the relative intrusion depth predicted by the short descent approximation. The simulation results show very good agreement with the experiments, and they closely track the short descent approximation for the reference case $Re = 15,000$, $m = 0.0744$, $v_s = 0.001$ for all tested stratifications.

Despite the limited size of the numerical domain, long descents—in the sense of large variation in current density—can be investigated through a parametric study of the settling



velocity. Figure 9a shows the particle concentration at $t = 15$ for various settling velocities v_s . Since the density of the head decreases for higher settling velocities, the flow intrudes earlier and higher along the slope, as marked by the dashed-line. Below we will compare predictions by the various scaling laws to simulation results. Towards this end, we also recall the long descent scaling law proposed by Snow and Sutherland [23] in the form

$$\left[1 + \frac{E}{2m} \left(\frac{H_i^2}{h_0^2} - 1 \right) \right]^{-\gamma-1} = S \frac{H_i}{h_0}, \tag{22}$$

where γ is the ratio of the particle-settling speed to the entrainment speed defined by

$$\gamma = \frac{v_s}{\bar{U}_e} = \frac{v_s}{E \cdot \bar{U}_f}. \tag{23}$$

In the numerical simulations, we expect settling to have a more dominant effect on the density of the current than entrainment in cases of large settling velocity and small intrusion depth. In the following, we propose two scaling relations for intrusion depth. In the first, we assume a well-mixed current of concentration c and constant volume $V = \frac{h_0 L_l}{2}$, i.e. a purely kinematic model in which entrainment is neglected, so that we have

$$\frac{h_0 L_l}{2} \frac{dc}{dt} = -v_s c L_c. \tag{24}$$

where $L_c(t)$ is the horizontal length of the current in contact with the slope. With \bar{U}_f the average front velocity before intrusion, we have $L_c(t) \approx L_l + \bar{U}_f t$ where we recall that L_l is the initial lock-length. For a constant settling velocity and with $c(t = 0) = 1$, we thus obtain, by integrating,

$$c(t) = e^{-2 \frac{v_s}{h_0} \left(t + \frac{1}{2} \frac{\bar{U}_f t^2}{L_l} \right)}. \tag{25}$$

This is the concentration of the current under the assumption that no entrainment occurs and the volume of the current thus remains constant. The density balance between the ambient fluid and the current at the intrusion depth takes the form

$$\rho_0 + c_{H_i}(\rho_1 - \rho_0) = \rho_T + (\rho_B - \rho_T) \frac{H_i}{H}, \tag{26}$$

where $c_{H_i} = c(t_i)$, with t_i being the time to intrusion. This can be related to the average front speed as

$$t_i = \frac{L_c - L_l}{\bar{U}_f} = \frac{H_i - h_0}{\bar{U}_f \tan \theta}. \tag{27}$$

Here, we use the fact that after the before intrusion, the Froude number Fr is independent of v_s , as shown in 4a. Recasting Eq. 26 and introducing 27 yields the condition for H_i/h_0

$$e^{-\frac{v_s}{\bar{U}_f \tan \theta} \left(\left(\frac{H_i}{h_0} \right)^2 - 1 \right)} - \frac{\rho_T - \rho_0}{\rho_1 - \rho_0} - \frac{\rho_1 - \rho_T}{\rho_1 - \rho_0} S \frac{H_i}{h_0} = 0. \tag{28}$$

This condition reduces to the short-descent approximation when $v_s = 0$. This equation can then be solved for H_i to give a prediction for the intrusion depth, and it is expected to work best in cases where settling dominates over entrainment in the change in current density.

The second model for intrusion depth incorporates entrainment similarly to [23], but in a way that explicitly separates the contributions of settling and entrainment-driven volume expansion. The change in current volume is given by

$$\frac{dh_c L_c}{dt} = L_c U_e \tag{29}$$

where $h_c(t) = h_0/2 + dh_c$ is the current height, which is assumed to be half the initial lock height upon release. Integrating to solve for h_c , we find

$$h_c = \frac{h_0}{2} + \frac{U_e t}{t_l + t} \left(\frac{1}{2} t + t_l \right), \tag{30}$$

where $t_l = \frac{L_l}{U_j}$ is defined for convenience. Assuming as previously that the current is homogeneous in concentration, but considering the change in volume due to entrainment, particle mass conservation yields, in terms of the particle mass $m_p = ch_c L_c$,

$$\frac{dm_p}{dt} = -v_s \frac{m_p}{h_c}, \tag{31}$$

such that

$$m_p = m_{p,0} e^{-v_s \int_0^t \frac{dt}{h_c(t)}}. \tag{32}$$

The particle concentration of the current at time t is thus given by

$$c = \frac{m_p}{m_{p,0}} \frac{h_0 L_l}{2 h_c L_c} = \frac{1}{2} \frac{h_0 t_l e^{-v_s \int_0^t \frac{dt}{h_c(t)}}}{\left[\frac{h_0}{2} + \frac{U_e t}{t_l + t} \left(\frac{1}{2} t + t_l \right) \right] [t + t_l]}, \tag{33}$$

where we used that $m_{p,0} = c_0 \frac{h_0 L_l}{2}$ and $c_0 = 1$ is the initial non-dimensional particle concentration in the lock. Note that the numerator can be integrated analytically but the resulting expression is cumbersome to work with, so that the integration is done numerically. At this point, we note that the scaling proposed by [23] does not account for the change in density of the entrained ambient fluid with depth. This assumption can become restrictive when the initial contribution of the particles to the lock-fluid density is comparable to that of the salt in the ambient fluid. We therefore propose one model referred to as HSE (Homogeneous Settling with Entrainment) that assumes that the entrained fluid has density ρ_0 equal to the interstitial density of the fluid as in [23], and one model referred to as HSEC (Homogeneous Settling with Entrainment Corrected) that calculates the density of entrained ambient fluid as a function of current depth. In the former, the intrusion condition is given by Eq. 26 with c given by Eq. 33. In the latter, the interstitial fluid density is a result of both the change in current volume and density of entrained fluid. This density is derived from the salt mass conservation equation

$$\frac{d\rho_i V}{dt} = \bar{U}_e \rho_e L_c, \tag{34}$$

where $V = h_c L_c$ is the current volume and ρ_i and ρ_e are the interstitial fluid density within the current and the entrained ambient fluid density respectively. ρ_e is approximated by the density in the ambient at the top of the current head, i.e. the density of the ambient at depth $L_c \tan \theta - h_0/2$. ρ_e can thus be approximated to leading order as

$$\rho_e = \rho_T + (\rho_B - \rho_T) \frac{L_c \tan \theta - h_0/2}{H} = \rho_T + (\rho_B - \rho_T) \frac{\bar{U}_f t + L_l/2}{H} \tan \theta. \tag{35}$$

Integrating Eq. 34 in time yields

$$\rho_i(t) = \frac{1}{V} \left[\rho_{i,0} V_0 + \bar{U}_e \bar{U}_f \left(\rho_T \left(\frac{t^2}{2} + t_l t \right) + (\rho_B - \rho_T) U_f t \left(\frac{t^2}{3} + \frac{3tt_l}{4} + \frac{t_l^2}{2} \right) \tan \theta \right) \right].$$

The HSEC intrusion condition therefore becomes

$$\rho_i(t_i) + c_{H_i}(\rho_1 - \rho_0) = \rho_T + (\rho_B - \rho_T) \frac{H_i}{H}. \tag{36}$$

Figure 9b, c present the computed intrusion depth as a function of settling velocity, the short descent approximation (SD), the so-called homogeneous settling approximation (HS) of Eq. 28 the homogeneous settling approximation with entrainment (HSE), the homogeneous settling approximation with entrainment corrected for entrained fluid density (HSEC) and the long descent approximations (LDA). The intrusion depth for the HSE, HSEC and LDA approximations was computed using a constant entrainment of $E = 0.01$, consistent with [23] for slopes of 0.0744 (Fig. 9b) and with entrainment of $E = 0.002$ (Fig. 9c)

At $v_s = 0$, the simulations agree well with the short-descent approximation. This corroborates that the numerical setup is effectively made into a long-descent system by means of increasing settling, not by allowing for entrainment to act for long times. The Homogeneous Settling (HS) approximation reduces to the short descent approximation in the absence of settling and agrees well quantitatively with the measured intrusion depth, although it consistently underestimates H_i for moderate settling velocities. The absence of entrainment in this model can lead to an overestimation of the particle-concentration at the slope which in turns leads to an overestimation of the density loss within the current, hence under-predicting intrusion depth. The LDA, HSE and HSEC all depend on the entrainment coefficient. For the constant value of $E = 0.01$, the LDA alternatively underestimates and overestimates the intrusion depth depending on the settling velocity, and the evolution of H_i with v_s using the LDA appears to be quasi-linear but does not reproduce the measurements of the numerical simulations. Both the HSE and HSEC agree well with the measurement at $v_s = 0.01$, but underpredict the intrusion depth at lower settling velocities. The HSEC, which accounts for the change in entrained ambient fluid density, performs much better than the HSE approximation, and suggests that the assumption of constant interstitial density made by [23] in the LDA is not always applicable. The results obtained with the LDA, HSE and HSEC suggest that the constant entrainment coefficient of $E = 0.01$ leads to an overestimation of the dilution of the current and thus leads to erroneous predictions of H_i . Quantitatively, the HS and HSEC methods produce errors that are within 20% of the measured intrusion depth for all values of v_s . An entrainment coefficient of $E = 0.002$ (Fig. 9c) was additionally used and shows far better agreement of all E -dependent predictions. In particular, the LDA leads to a reduced error at small settling velocities but overestimates the intrusion depth at larger settling velocities. At $E = 0.002$, the HSEC yields qualitatively satisfying results over the whole range of tested settling velocities. The results

are almost identical to the HS approximation although this is purely coincidental as HSEC depends on both entrainment and density of entrained fluid.

In summary, the case of long descents in the sense of strong settling and low entrainment proves particularly challenging for prediction of the intrusion depth. The LDA is particularly sensitive to the choice of entrainment coefficient E and diverges from the measurements as v_s increases. The HSE reduces to the HS as entrainment approaches zero, but underestimates intrusion depth in all tested cases. The HSEC behaves more similarly to the measured intrusion depth as settling increases but also depends strongly on entrainment. The simpler approximation HS that neglects entrainment and solely focusses on settling-induced density changes provides robust agreement with the measured data. For practical applications, given a certain front velocity \bar{U}_f , lock geometry and slope, the sensitivity of each individual method to the entrainment coefficient should be explored before providing any estimate for the intrusion depth. The HSEC provides an alternative to the LDA which should be further explored with longer-descent, variable slope, numerical simulations.

5 Energy budget

Turbidity currents convert potential energy into kinetic energy, which is subsequently dissipated via viscous friction by the resolved small-scale structures of the flow and the unresolved Stokes flow around each settling particle [20]. Numerical simulations allow us to calculate all of these components of the energy budget, so that the effects of slope and stratification on the energy budget can be assessed. We refer to [20] for a comprehensive derivation of the energy budget. As particles settle on a slope, an additional contribution to the energy budget appears in the form of a settled particle potential energy. The average energy conservation equation writes as

$$E_{p,tot} + E_k + L = const., \tag{37}$$

where $E_{p,tot}$ is the total potential energy, E_k is the total kinetic energy and L is the total time-integrated losses. The total potential energy is comprised of the potential energies associated with salt ($E_{p,s}$), particle concentration ($E_{p,c}$) and deposited particles ($E_{p,dep}$) such that $E_{p,tot} = E_p + E_{p,dep} = E_{p,c} + E_{p,s} + E_{p,dep}$, where

$$E_{p,c}(t) = \alpha_c \int_{\Omega} cy \cdot dV, \tag{38}$$

$$E_{p,s}(t) = \alpha_s \int_{\Omega} sy \cdot dV, \tag{39}$$

$$E_{p,dep}(t) = \alpha_c \int_x \int_z c_{dep}(x, z, t) \cdot y_s(x) dx dz. \tag{40}$$

The total kinetic energy E_k , is given by

$$E_k(t) = \int_{\Omega} \frac{1}{2} u_i u_i dV. \tag{41}$$

The total loss is $L = L_v + L_s$ is the sum of viscous losses L_v and losses due to the Stokes flow around the settling particles L_s , where

$$L_v(t) = \int_t \epsilon(t)dt, L_s(t) = \int_t \epsilon_s(t)dt, \quad (42)$$

and

$$\epsilon = \int_{\Omega} \frac{2}{Re} s_{ij} s_{ij} dV, \quad \epsilon_s = \alpha_c v_s \int_{\Omega} cdV. \quad (43)$$

To improve readability of the plots, the potential energies are calculated relatively to their initial values, i.e. $\Delta E_{p,i}(t) = E_{p,i}(t) - E_{p,i}(0)$.

For clarity, the energy budget is divided into two steps. First, the overall budget of potential energy variation, kinetic energy variation and losses is presented. Then, the different components of potential energy, kinetic energy and losses are separately plotted. Figure 10a represents the overall energy budget associated with a typical set-up ($Re = 15,000$, $S = 0.419$, $m = 0.0744$, $v_s = 0.001$). The overall potential energy steeply decreases at early times as it is converted into kinetic energy. The kinetic energy quickly reaches a maximum and then slowly decreases under the effect of dissipation. It also decreases as it is converted back into potential energy. Indeed, the current has to lift the linearly stratified ambient fluid, increasing the salt potential energy at the expense of kinetic energy. Note that the overall energy, while not conserved exactly, remains constant to a very good degree.

Note also that the potential energy starts increasing at later times ($t > 12$), after the intrusion of the current into the ambient fluid. This can be understood by looking at the potential energy budget components, presented in Fig. 10b. While the potential energy of the particles keeps decreasing, a substantial amount of the lock's initial potential energy is converted back from kinetic energy into potential energy by lifting of the stratified ambient fluid, as mentioned previously. The salt potential energy therefore increases as the current moves down the slope.

Figure 10c shows the time evolution of viscous and Stokes dissipation losses. Viscous losses reach a maximum slope during intrusion, indicating a maximum of instantaneous viscous dissipation. Stokes losses due to particle settling account for a small fraction of the total losses at such small settling velocities and appear to be a linear function of time. This emphasises that particle mass at small settling velocities remains almost constant on the time scale leading to intrusion. As pointed out by Necker et al. [20], the proportion of losses due to Stokes dissipation testifies to how much of the initial energy could actually be used to create motion and transport, including mixing and modification of the ambient fluid stratification; and by contrast of how much was lost to particle settling. However, the ratio of viscous to Stokes losses strongly depends on stratification and settling speed, as illustrated in Fig. 10d, e respectively.

The increase in stratification leads to a decrease in potential energy available for conversion into kinetic energy, and thus to a strong decrease in viscous dissipation (Fig. 10d). Necker et al. [20] observed that the contributions of Stokes and viscous losses in a turbidity current on a flat bottom were approximately the same. This observation does not hold in the case of a turbidity current down a slope into a stratified ambient fluid. In the critical case of $S \rightarrow 1$, the problem reduces to a turbidity current on a flat bottom with stratification and both loss contributions are expected to be of the same order. This is indeed verified for $S = 0.692, 1.028$, but only holds true for this particular settling velocity. The losses as a function of time for various settling velocities are computed with $S = 0.419$ (Fig. 10e). The increase in settling velocity leads to a faster decrease in concentration that translates to a loss of buoyancy forces, kinetic energy and eventually viscous losses. The increase in

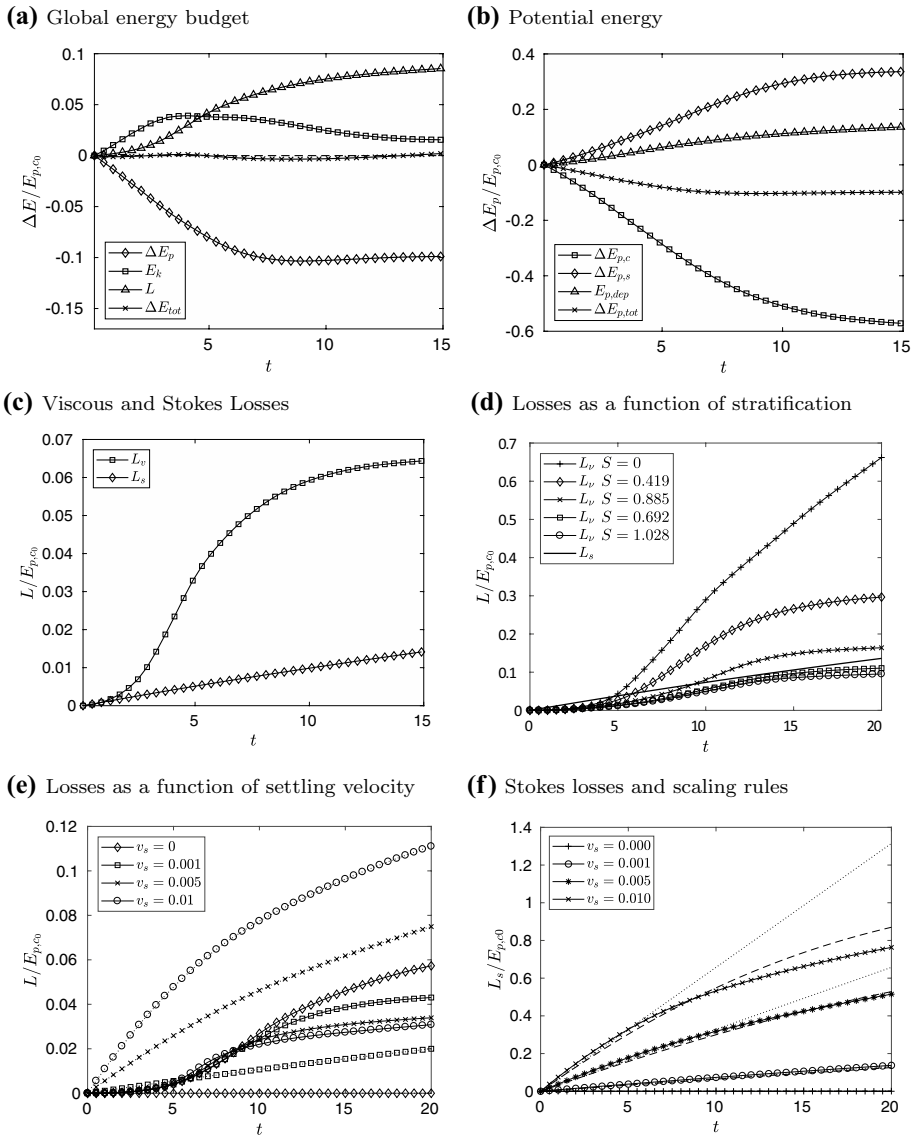


Fig. 10 Energy budget as a function of time: **a-c** ($Re = 15,000$, $S = 0.419$, $v_s = 0.001$, $m = 0.0744$): **a** variation of the total, potential and kinetic energy and dissipation losses; **b** variation of total, particle, salt and deposited potential energy; **c** viscous and Stokes dissipation losses. **d** ($Re = 15,000$, $S = 0, 0.419, 0.692, 0.885, 1.028$, $v_s = 0.001$, $m = 0.0744$) Viscous and Stokes dissipation losses for various stratifications; **e-f** ($Re = 15,000$, $S = 0.419$, $m = 0.0744$, $v_s = 0, 0.001, 0.005, 0.01$) **e** viscous and Stokes dissipation losses for various settling velocities; **f** Stokes dissipation losses (full line with markers) and linear (dotted line) and non-linear (dashed line) scalings

settling velocity leads to an increase in Stokes losses, as expected, but additionally leads to a non-linear behaviour. This shows that for large settling velocities, the Stokes losses can overcome viscous losses and the mass of suspended particles decreases sufficiently rapidly

that Stokes losses decrease noticeably with time. Stokes losses can be estimated by first assuming a constant suspended mass, which is expected to be a valid assumption for flows with small particle settling velocities. This linear model writes as

$$L_{s,lin} = \alpha_c v_s V_{lock} t, \quad (44)$$

where $V_{lock} = \frac{1}{2} h_0 L_l$ is the initial volume of the lock per unit width at concentration $c = 1$. A second model is proposed where the change in particle concentration is taken into account, following the derivations of the HS intrusion model of Eq. 25. The Stokes losses $L_{s,nl}$ in this model are thus given by

$$L_{s,nl} = \alpha_c V_{lock} v_s \int_0^t \int_{\Omega} e^{-2 \frac{v_s}{h_0} \left(t + \frac{1}{2} \frac{U_f t^2}{L_l} \right)} dV dt. \quad (45)$$

The linear (dotted line) and homogeneous settling (dashed line) scaling laws for Stokes losses are plotted against the computed Stokes losses (full line and markers) in Fig. 10f. Both scaling laws are a perfect match at low settling velocities ($v_s = 0.001$), as expected. At larger settling velocities, the linear law fails to capture changes in suspended mass and therefore overestimates the Stokes losses. The non-linear model yields an excellent match with the measured dissipation, even at the highest settling velocity, thus providing confidence in the ability of the HS model to predict the mean particle concentration within the current.

In summary, in a stratified ambient fluid with sufficiently large settling velocities, dissipation processes are dominated by drag losses on the settling particles. The initial potential energy available for conversion into kinetic energy strongly depends on the settling speed, and Stokes losses can represent the most important source of dissipation, and be the driving mechanism for density change in the current leading up to intrusion.

6 Conclusion

The behaviour of turbidity currents down a slope into a stratified ambient fluid was analysed through highly resolved numerical simulations. The general three-dimensional behaviour of the flow was discussed before quantitatively investigating its dynamic properties. Results were compared to experimental data, confirming the ability of numerical simulations to capture the experimentally observed flow dynamics.

The computed front velocity agrees well with experimental results under varying stratification and settling speed. This allows for the introduction of a combined scaling law for the front velocity based on two well known theoretical limits. Numerical data quantitatively matches the new scaling law, so that it can be used to predict the front velocity plateau of more realistic down-slope turbidity currents in a stratified ambient fluid.

Entrainment of ambient fluid into the current was investigated through a time dependent and local approach, allowing for a time and space resolved description of entrainment processes. The entrainment was found to be highly variable with time and over the length of the current. The local variability relates to large turbulent structures in the head and tail while the space-averaged time dependence relates to the variation in turbulent kinetic energy as the flow develops and then intrudes. Averaged values of the entrainment were found to agree well with experimental data and were an even better match to theoretical results. Both the high variability of entrainment and the ability of numerical simulations to

capture it suggest that it should be used as a verification tool in the investigation of intrusion depth rather than a predictable quantity.

The influence of stratification and settling velocity on intrusion depth was analysed. Numerical results showed very good agreement with the short descent approximation in cases of large stratification and small settling velocities, as expected. High settling scenarios that depart from the constant concentration approximation of the short descent are more challenging to predict. A new scaling law based on the assumption of a homogeneous, constant volume current (HS) was proposed. This model was refined to incorporate entrainment (HSE), but the assumption of a homogeneous current yielded under prediction of the intrusion depth and proved sensitive to the chosen entrainment coefficient. Finally, a model that takes into account the change in density of the entrained ambient fluid (HSEC) was proposed and yielded satisfying results when compared to the measured intrusion depth, particularly for such low-entrainment situations. Sensitivity to entrainment coefficient in low entrainment and high settling scenarios is observed even more strongly using the long-descent approximation (LDA) of [23]. In this context, the HS approximation provides a valuable tool for estimating the intrusion depth solely based on settling. In future work, we hope to see the HSEC applied to longer descent scenarios and compared to the LDA of [23].

The energy budget of the flow highlights the effect of stratification on energy transfer from potential energy into kinetic energy and back into potential energy of the ambient fluid. Stratification directly affects the production of kinetic energy and thus the amount of viscous dissipation, mixing and finally entrainment that occurs at the current-ambient interface. In high stratification conditions ($S \approx 1$), this means that settling can become the dominant source of energy losses in the propagating current and thus that settling most strongly affects the density of the current prior to intrusion. The HS model for current concentration is applied to predict the Stokes settling losses as a function of time for various settling velocities and is shown to accurately capture the effect of the drop is suspended mass on Stokes losses. This further validates the approach of concentration modelling in the HS approximation, and suggests that inaccuracies in the prediction of the intrusion depth can be attributed to the sensitivity of the model to the entrainment coefficient.

Acknowledgements We thank Dr. Senthil Radhakrishnan for his significant input during the early stages of this project. EM gratefully acknowledges support from the Army Research Office, under Grant W911NF-18-1-0379.

References

1. Beghin P, Hopfinger EJ, Britter RE (1981) Gravitational convection from instantaneous sources on inclined boundaries. *J Fluid Mech* 107(1):407. <https://doi.org/10.1017/S0022112081001821>
2. Benjamin TB (1968) Gravity currents and related phenomena. *J Fluid Mech* 31(2):209–248. <https://doi.org/10.1017/S0022112068000133>
3. Britter RE, Linden PF (1980) The motion of the front of a gravity current travelling down an incline. *J Fluid Mech* 99(03):531. <https://doi.org/10.1017/S0022112080000754>
4. Cantero MI, Balachandar S, García MH, Bock D (2008) Turbulent structures in planar gravity currents and their influence on the flow dynamics. *J Geophys Res Oceans* 113(C8):1. <https://doi.org/10.1029/2007JC004645>
5. Cantero MI, Lee JR, Balachandar S, García MH (2007) On the front velocity of gravity currents. *J Fluid Mech* 586:1–39. <https://doi.org/10.1017/S0022112007005769>
6. de Rooij F (2000) Sedimenting particle-laden flows in confined geometries. Ph.D. thesis, University of Cambridge

7. de Rooij F, Dalziel SB (2001) Time- and space-resolved measurements of deposition under turbidity currents. In: McCaffrey W, Kneller B, Peakall J (eds) *Particulate gravity currents*. Blackwell Publishing Ltd, Hoboken, pp 207–215
8. de Rooij F, Linden PF, Dalziel SB (1999) Saline and particle-driven interfacial intrusions. *J Fluid Mech* 389:303–334
9. Fadlun E, Verzicco R, Orlandi P, Mohd-Yusof J (2000) Combined immersed-boundary finite-difference methods for three-dimensional complex flow simulations. *J Comput Phys* 161(1):35–60. <https://doi.org/10.1006/jcph.2000.6484>
10. Gualtieri C, Angeloudis A, Bombardelli F, Jha S, Stoesser T (2017) On the values for the turbulent Schmidt number in environmental flows. *Fluids* 2(2):17. <https://doi.org/10.3390/fluids2020017>
11. Hallworth MA, Huppert HE, Phillips JC, Sparks RSJ (1996) Entrainment into two-dimensional and axisymmetric turbulent gravity currents. *J Fluid Mech* 308:289–311. <https://doi.org/10.1017/S0022112096001486>
12. Härtel C, Carlsson F, Thunblom M (2000) Analysis and direct numerical simulation of the flow at a gravity-current head. Part 2. The lobe-and-cleft instability. *J Fluid Mech* 418:213. <https://doi.org/10.1017/S0022112000001270>
13. Härtel C, Meiburg E, Necker F (2000) Analysis and direct numerical simulation of the flow at a gravity-current head. Part 1. Flow topology and front speed for slip and no-slip boundaries. *J Fluid Mech* 418:189–212. <https://doi.org/10.1017/S0022112000001221>
14. Kang S (2008) An improved immersed boundary method for computation of turbulent flows with heat transfer. Ph.D. thesis, Stanford University
15. Meiburg E, Kneller B (2010) Turbidity currents and their deposits. *Ann Rev Fluid Mech* 42:135–156. <https://doi.org/10.1146/annurev-fluid-121108-145618>
16. Mittal R, Iaccarino G (2005) Immersed boundary methods. *Ann Rev Fluid Mech* 37(1):239–261. <https://doi.org/10.1146/annurev.fluid.37.061903.175743>
17. Nasr-Azadani M, Meiburg E (2011) TURBINS: an immersed boundary, Navier–Stokes code for the simulation of gravity and turbidity currents interacting with complex topographies. *Comput Fluids* 45(1):14–28. <https://doi.org/10.1016/j.compfluid.2010.11.023>
18. Nasr-Azadani MM, Meiburg E, Kneller B (2016) Mixing dynamics of turbidity currents interacting with complex seafloor topography. *Environ Fluid Mech* 18:1–23. <https://doi.org/10.1007/s10652-016-9477-9>
19. Necker F, Härtel C, Kleiser L, Meiburg E (2002) High-resolution simulations of particle-driven gravity currents. *Int J Multiph Flow* 28(2):279–300. [https://doi.org/10.1016/S0301-9322\(01\)00065-9](https://doi.org/10.1016/S0301-9322(01)00065-9)
20. Necker F, Härtel C, Kleiser L, Meiburg E (2005) Mixing and dissipation in particle-driven gravity currents. *J Fluid Mech* 545:339–372. <https://doi.org/10.1017/S0022112005006932>
21. Parsons JD, Bush JWM, Syvitski JPM (2001) Hyperpycnal plume formation from riverine outflows with small sediment concentrations. *Sedimentology* 48(2):465–478. <https://doi.org/10.1046/j.1365-3091.2001.00384.x>
22. Rimoldi B, Alexander J, Morris S (1996) Experimental turbidity currents entering density-stratified water: analogues for turbidites in mediterranean hypersaline basins. *Sedimentology* 43(3):527–540. <https://doi.org/10.1046/j.1365-3091.1996.d01-21.x>
23. Snow K, Sutherland BR (2014) Particle-laden flow down a slope in uniform stratification. *J Fluid Mech* 755:251–273. <https://doi.org/10.1017/jfm.2014.413>
24. Tseng YH, Ferziger JH (2003) A ghost-cell immersed boundary method for flow in complex geometry. *J Comput Phys* 192(2):593–623. <https://doi.org/10.1016/j.jcp.2003.07.024>
25. Ungarish M (2006) On gravity currents in a linearly stratified ambient: a generalization of Benjamin's steady-state propagation results. *J Fluid Mech* 548:49–68. <https://doi.org/10.1017/S0022112005007421>
26. Ungarish M (2009) *An introduction to gravity currents and intrusions*. Chapman and Hall/CRC, Boca Raton. <https://doi.org/10.1201/9781584889045>

Publisher's Note Springer Nature remains neutral with regard to jurisdictional claims in published maps and institutional affiliations.